PNAS RESEARCH ARTICLE | NEUROSCIENCE

Hierarchical whole-brain modeling of critical synchronization dynamics in the human brain

Vladislav Myrov[a,1], Alina Suleimanova[a], Samanta Knapič[a,b], Paula Partanen[b,c], Maria Vesterinen[b,d], Wenya Liu[a,b], Satu Palva[b,e], and J. Matias Palva[a,b,e,1]

Affiliations are included on p. 11.

Edited by Wolf Singer, Ernst-Strungmann-Institut gGmbH, Frankfurt am Main, Germany; received April 24, 2025; accepted January 20, 2026

The brain operates at the critical transition between order and disorder which supports optimal information processing. Whole-brain computational modeling is a powerful tool for uncovering the system-level mechanisms behind large-scale brain activity in both healthy and pathological states. However, most previous approaches have focused on either functional connectivity or criticality, making it difficult to capture both aspects simultaneously. Here, we introduce a method based on a Hierarchical Kuramoto model that incorporates two levels of hierarchy. In our model, each node contains a large number of coupled oscillators, which allows us to examine both local synchronization and long-distance interactions between brain regions. The model produces critical-like dynamics marked by emergent long-range temporal correlations (LRTCs) and both interareal phase synchronization and amplitude cross-correlations (CC) during the transition from asynchronous to synchronous states. Notably, structure–function coupling shows distinct patterns: correlations with structural connectivity peak at criticality for LRTCs and CC, but decay for local and interareal phase synchronization. Comparisons with human resting-state magnetoencephalography (MEG) data reveal that the model's behavior most closely resembles MEG phase synchronization and multipeak power spectra on the subcritical side of an extended critical regime, supporting the hypothesis that the human brain operates in this state.

brain oscillations | criticality | computational modeling | kuramoto | MEG

Electrophysiological brain activity is characterized by neuronal oscillations—rhythmic excitability fluctuations arising with frequency-specific synaptic mechanisms in neuronal micro- and macrocircuits (1). Human brains in vivo exhibit moderate levels of long-range phase synchronization of neuronal oscillations in both intracerebral stereo-EEG (iSEEG) (2, 3) and noninvasive magneto- and electroencephalographic (M/EEG) recordings (4–6). Synchronization plays a mechanistic role in regulating neuronal communication in distributed brain networks (7–9) underlying cognitive functions (10–12). In contrast, both hypo- and hypersynchronization constitute core pathophysiological mechanisms in neurological disorders including epilepsy (3, 13), Parkinson's disease (14), as well as in neuropsychiatric diseases, e.g., depression (15).

Electrophysiological methods such as M/EEG and SEEG in humans (Fig. 1*A*) provide millisecond-scale temporal resolution required to observe oscillations in frequency ranges from 1 to >200 Hz. Typically, data from these recordings are filtered to obtain narrow-band analytic time series (Fig. 1*B*) and observables, such as local power spectra (Fig. 1*C*), and amplitude time series are then used as proxy measures for local (within-parcel) neuronal synchronization. Functional connectivity (FC) of interareal interactions could be estimated with pairwise interareal amplitude correlation (Fig. 1 *D* and *F*) and phase synchronization (Fig. 1 *E* and *G*), or their multivariate counterparts. Neuronal oscillations exhibit remarkable variability across individuals in their power and levels of interareal coupling. This variability is functionally significant as it explains, e.g., difference in cognitive performance (16) and neurological state (13).

The framework of criticality provides a statistical physics perspective to understanding these neuronal dynamics and their variability. The "critical brain" hypothesis (17–20) proposes that the operating point (OP) of neuronal systems in vivo lies at the phase transition between subcritical (disordered) and supercritical (ordered) phases in the system's state space. Operation at this critical point leads to the emergence of scale-free spatiotemporal correlations, observable both as long-range temporal correlations [LRTCs, (18)] and power-law scaled avalanches (19), and yields several functional advantages,

Significance

Nested neuronal networks exhibit scale-free activity in vivo, but there is a shortage of mechanistic models linking such hierarchical architectures with measurable dynamics. We advance here a Hierarchical Kuramoto model that directly links local and interareal synchronization dynamics with neuroimaging observables. The model revealed an extended regime of critical-like dynamics with in-vivo like long-range temporal correlations, avalanche dynamics, and functional connectivity. We found unique forms of structure–function coupling, maximization of model-experiment similarity, and emergence of multifrequency balance in this regime. These results suggest that resting-state brain activity operates largely on the subcritical side of an extended critical regime and show how anatomical hierarchy and heterogeneous coupling shape large-scale dynamics.

Author contributions: W.L. preprocessed the MEG data; P.P. and M.V. collected the MEG data; S.P. and J.M.P. curated the study; V.M. and J.M.P. designed research; V.M. performed research; V.M. contributed new reagents/analytic tools; V.M. and A.S. analyzed data; S.K. preprocessed the DWI data; and V.M., A.S., S.K., P.P., M.V., W.L., S.P., and J.M.P. wrote the paper.

The authors declare no competing interest.

This article is a PNAS Direct Submission.

[1] To whom correspondence may be addressed. Email: vladislav.myrov@aalto.fi or matias.palva@aalto.fi.

This article contains supporting information online at https://www.pnas.org/lookup/suppl/doi:10.1073/pnas.2505768123/-/DCSupplemental.

Published March 17, 2026.

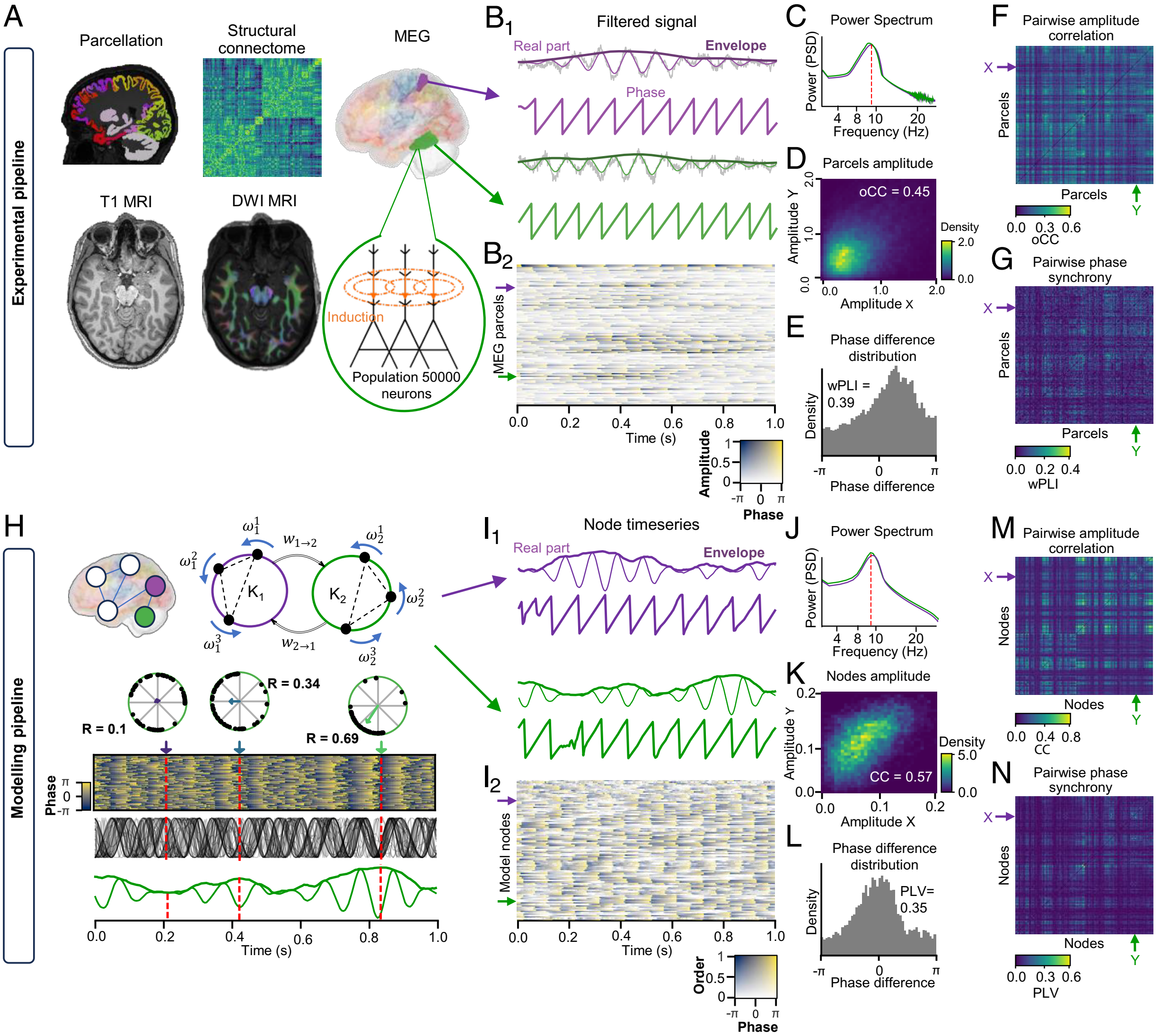

Fig. 1. General representation of an experimental pipeline. (*A*) Summary of imaging and data processing methods, with T1-weighted MRI (MRI) for anatomical parcellation, Diffusion-weighted imaging (DWI) MRI for structural connectome reconstruction, and MEG for functional data acquisition. (B_1) MEG signals from the two representative parcels in (*A*) showing the broadband signal (gray) overlaid with the narrow-band filtered signal at 10 Hz, its phase and envelope. (B_2) Phase heatmap of MEG signals across channels, with low-amplitude regions shown as transparent. (*C*) Power spectral density (PSD) for the two parcels. (*D*) Two-dimensional histogram of amplitudes for the 10 Hz parcel signals in (*B*). (*E*) Distribution of phase differences between a pair of MEG signals, with a weighted phase lag index (wPLI) of 0.39. (*F*) Heatmap of pairwise orthogonalized amplitude correlations (oCC) of alpha-band MEG signals (10 Hz). (*G*) Pairwise wPLI matrix of alpha-band MEG signals (10 Hz). Modeling pipeline. (*H*) On top level, the model is made of multiple interconnected nodes where each node represents a single brain region. Each node comprises a large amount of Kuramoto oscillators with central frequency ω and intranodal coupling strength of K_n. The complex average across oscillators yields the node time series of which the absolute value is node order (R) that is comparable with oscillation amplitude in MEG (*B*). I_1 Node time series and corresponding phase I_2 for two model nodes. (*J*) Power spectral density of the real part of simulated time series. (*K*) Two-dimensional histogram of amplitudes for two simulated signals. (*L*) Phase difference distribution for two simulated signals, with an example PLV value of 0.35. (*M*) Pairwise amplitude correlation heatmap for simulated time series. (*N*) Pairwise PLV matrix of simulated signals.

including maximized information capacity (20), complexity (21), dynamic range (22), and transmission rate (23).

OP indicates the system's position in the state space and is regulated by underlying control parameters including the excitation–inhibition (E/I) balance that is maintained both by fast neurotransmission (24–26), slow neuromodulation (27, 28) where the ascending reticular arousal system is a potent dynamic modulator (29), and the topology of structural connectivity (SC) between brain areas (30, 31). A given OP is associated with specific emergent dynamics, which can be operationalized with a range of synchronization and criticality observables (18, 19, 25, 32–34). Because neither the control parameters nor the system's states are observable from measurement data, their relationships with observables have remained a topic of interest (35), whereas computational modeling is a useful method for studying the effect of system control parameters on its dynamics.

Numerous computational models have been developed to investigate the principles underlying whole-brain neural dynamics (36–39). These models are made "whole-brain" relevant by connecting the model's nodes into a network with weights obtained from the structural connectome of human white-matter connections measured with diffusion tensor spectrum (40). Whole-brain scale neural dynamics has been modeled, e.g., with the Wilson–Cowan model (41), neural mass models (42), and the Kuramoto model (43). In particular, patterns of interareal functional connectivity have been addressed with neural mass models (44) and Hopf models (45), and have also been used as a neuronal correlation proxy for functional MRI (fMRI) (46, 47).

Computational models in criticality research have traditionally focused on neuronal avalanches using branching-process formulations (48), Ising models from statistical physics (49) or spiking models (50), which do not capture oscillatory phenomena such as synchronization dynamics. Models such as the critical oscillations (CROS) model, show that networks of excitatory and inhibitory neurons may also exhibit oscillations with emergent LRTCs and avalanche dynamics (25, 51, 52). Nevertheless, neuron-level models have been largely used to represent local populations rather than whole-brain-scale dynamics, and synchronization therein is an emergent phenomenon rather than an explicitly modeled mechanism. On a whole-brain scale, neurophysiology-inspired population models based on oscillators with intrinsic amplitude dynamics (53–55) have been shown to give rise to synchronization phenomena and can be tuned to operate in a region with metastable dynamics. However, evidence for criticality in these models, e.g., emergence of LRTCs, has remained limited.

The Kuramoto model is one of the foundational models of critical synchronization dynamics and captures the emergence of self-organized synchrony in a system of coupled oscillators (56). The model exhibits a phase transition between subcritical (asynchronous) and supercritical (synchronous) phases, which is characterized by emergence of critical-like dynamics, such as LRTCs (32) and avalanches (57). Prior research using Kuramoto modeling in the neuroscience context has represented the activity of neuronal populations within cortical areas with single Kuramoto oscillators coupled by realistic interareal SC (58). This approach thus provides insight into whole-brain network dynamics but does not yield node-level observables, such as order fluctuations or LRTCs, which are essential markers for critical dynamics. Another approach for using the Kuramoto model represents a neuronal system as either a single (59, 60) or two large populations (61, 62) of oscillators, which captures critical-like dynamics at a “local” level similarly to the CROS model, but does not extend the model into structural-connectivity defined whole-brain scale networks. Therefore, there has remained a shortage of models that a) are directly comparable with large-scale recordings such as MEG or EEG in terms of scales and observables, b) capture local and interareal synchronization dynamics concurrently, and c) exhibit critical-like dynamics including LRTCs and avalanche dynamics.

We present here a hierarchical extension of the classic Kuramoto model. Hierarchical Kuramoto consists of a whole-brain network where each node itself is a system of a large number of oscillators. This two-level architecture yields separable local and interareal synchronization dynamics, and consequently also interareal order/amplitude correlation dynamics, which are not available in the classical “flat” Kuramoto model where a single population yields only either interareal phase synchronization (between oscillators) or local order dynamics (across oscillators). The hierarchical configuration is thus essential for enabling direct comparability with the local and interareal brain dynamics observables in neuroimaging data. We first established the emergence of LRTCs and avalanche dynamics in the Hierarchical Kuramoto model at criticality. We then used this model to investigate how structure–function coupling depends on the operating point of the system. Finally, to estimate the likely range of operating points in human brain dynamics, we asked where in the parameter space the emergent model dynamics best match the experimental multiscale dynamics and the power spectra observed with MEG.

Results

Whole-Brain Model of Critical Oscillations. Brain activity emerges through interactions on both micro- and macroscopic scales from small neuronal assemblies to large neuronal systems observable with noninvasive electrophysiological methods such as MEG (Fig. 1*A*). Complex interactions across micro to large scale dynamics give rise to oscillatory phenomena with the rich phase and amplitude dynamics at different time-scales (Fig. 1*B*), which are measurable, e.g., with observables such as power spectra (Fig. 1*C*), amplitude correlation (Fig. 1 *D* and *F*), and phase synchronization typically operationalized with phase locking value (PLV) or weighted phase-lag index (wPLI) (Fig. 1 *E* and *G*).

Synchronous postsynaptic currents in tens of thousands of pyramidal neurons in the cerebral cortex are the key generators of MEG and EEG signals, of which the amplitude reflects the degree of neuronal synchronization. It has been estimated that synchronization of these postsynaptic potentials accounts between 90 and 99% of the oscillation amplitude in MEG/EEG recordings (63–65). To concurrently capture and dissect intra- and interareal synchronization dynamics, we designed a two-level model where each node was a full system of Kuramoto oscillators (56), analogously to each cortical area containing a large population of neurons. The oscillators were directionally coupled within each node with coupling weighted by the local control parameter K (Fig. 1*H*, see *Materials and Methods* for details). These local synchronization dynamics, internal to each node (Fig. 1 *H* and *I*), were similar to the local neocortical synchronization dynamics observable in vivo MEG oscillation amplitude fluctuations (Fig. 1*B*) both phenomenologically and in terms of their observables. Because noninvasive electrophysiological methods primarily resolve only local and interareal dynamics, two levels represent the maximum hierarchical depth inferable with MEG/EEG data.

On the whole-brain level of hierarchy, we defined the interaction between the nodes with the directional phase-difference of respective complex node time series weighted by node order and strength of white-matter structural connections between the nodes (*Materials and Methods*). The local synchronization fluctuations (Fig. 1*I*) were paralleled by interareal FC in the forms of amplitude (order) correlations (Fig. 1 *K* and *M*) and phase synchrony (Fig. 1 *L* and *N*), again with phenomenological similarity with those observed in MEG data.

Although both empirical and modeling work indicates that conduction delays shape large-scale phase relations (66–68), we focused here on how local and global coupling strengths control oscillatory dynamics to limit the scope of the present study. Nonetheless, the flexible architecture of the model readily allows the inclusion of conduction delays and an implementation supporting them is available in the public repository.

Local and Global Control Parameters Shape the Model Critical–Like Dynamics. The critical brain hypothesis posits that neural networks in vivo operate near a critical point between order and disorder characterized by moderate levels of synchronization to optimize computational capabilities and adaptability (20, 24, 69). Such critical region in the state space emerges from a position in parameter space. In network models, these parameters could be local and global coupling strengths (Fig. 2*A*). A phase transition spans desynchronization to near-complete synchronization at both node and interareal levels, which is operationalized with node order and internode phase synchronization, respectively. The critical dynamics emerge at the phase transitions where oscillations are characterized by LRTCs, operationalized using

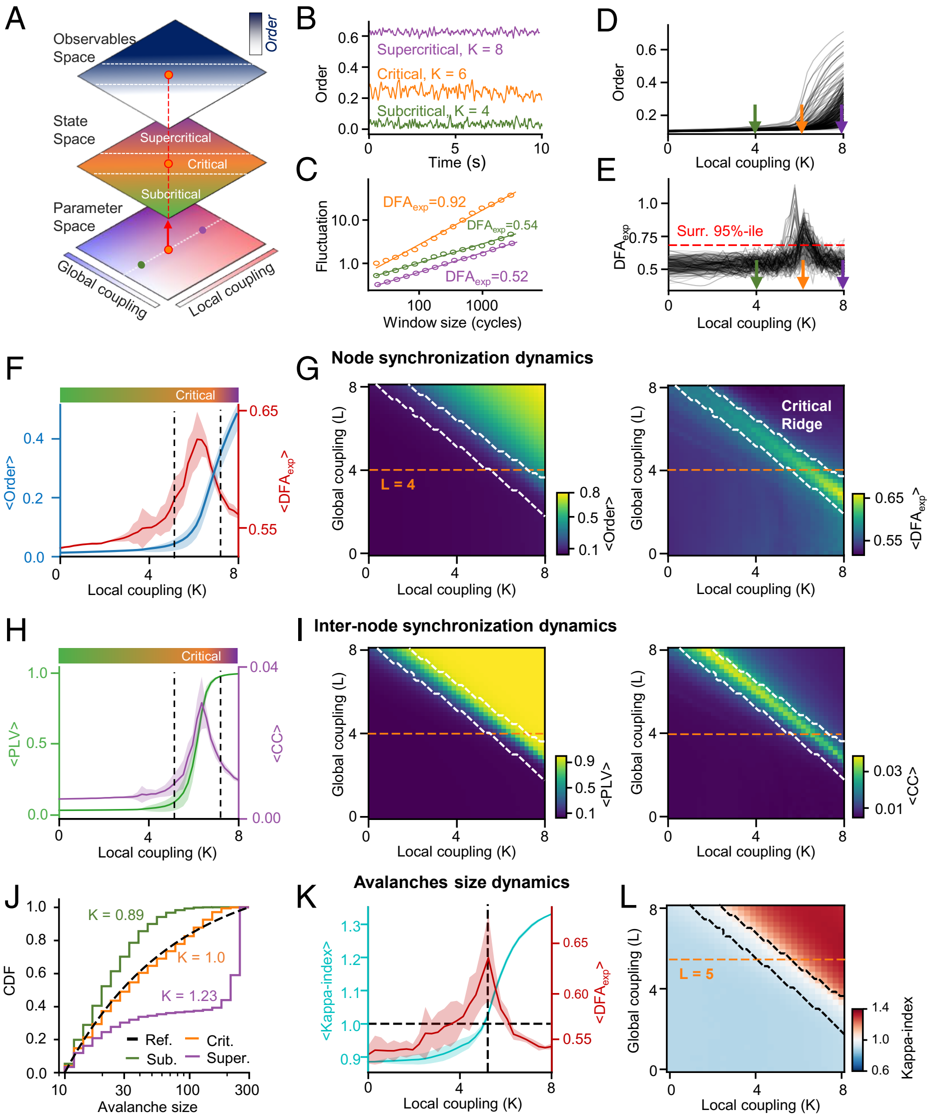

Fig. 2. Phase transition and emergence of critical-like dynamics in Hierarchical Kuramoto Model. (*A*) Simplified representation of the parameter space of two-level Hierarchical Kuramoto, illustrating two key control parameters: local coupling strength (K) and global coupling strength (L). Colored dots indicate three distinct parameter combinations giving rise to unique operating points in the subcritical, critical, and supercritical parts of the state space, leading to observables such as synchronization and long-range temporal correlations (LRTCs). (*B*) Exemplar time series generated with the model from subcritical, critical, and supercritical regimes states. (*C*) Detrended fluctuation analysis (DFA) fits and their exponents (DFA_{exp}) for each regime. (*D*) An average model order as a function of local coupling strength (K). One line represents a single model node. (*E*) DFA exponent (DFA_{exp}) as a function of local coupling strength (K), where each line represents a single model node. The red dashed line indicates a 95-th percentile of DFA exponent obtained from surrogate data (white noise). (*F*) Average model order (blue) and DFA_{exp} (red) as a function of local coupling strength (K). Dashed black lines indicate the critical ridge with average $DFA_{exp} \geq 0.6$. Shaded areas represent SE CI ($\pm \frac{SD}{\sqrt{N}}$, where $N = 24$ models). (*G*) Heatmaps of average order (*Left*) and DFA_{exp} (*Right*) across model nodes as functions of local (K) and global (L) coupling strengths. Dashed white lines indicate the critical ridge, defined as a region where average $DFA_{exp} \geq 0.6$. (*H*) Average Phase Locking Value (PLV, green) and cross-correlation (CC, purple) as functions of local coupling strength (K). (*I*) Heatmaps of PLV (*Left*) and CC (*Right*) averaged across edges, as functions of local (K) and global (L) coupling strengths. (*J*) CDF for the reference power-law distribution with scaling exponent = $\frac{-3}{2}$, subcritical, critical, and supercritical models. (*K*) κ-index and DFA_{exp} as a function of K. The horizontal black line indicates where κ-index equals 1, the vertical dashed black line indicates where DFA exponent peaks. (*L*) Heatmap of average κ-index as a function of both model control parameters. The dashed black lines indicate the critical region defined the same as in previous panels.

Detrended Fluctuation Analysis (DFA, Fig. 2 *B* and *C*) these peaking at the critical phase transition.

To assess the emergence of critical dynamics in our model, we first used a single-subject SC matrix to define interareal coupling weights (SC-informed model). We then simulated resting-state activity (see *SI Appendix* for details) and computed the DFA exponent for each node of the simulated time series as a function of the local coupling coefficient (K).

We found that the hierarchical approach effectively modeled the critical transition at the individual node level from low to high local synchronization (Fig. 2*D*). This transition featured a peak in the DFA scaling exponent near 1, indicating critical-like dynamics (Fig. 2*E*). Notably, LRTCs emerged across a range of model control parameters rather than at a single point. We define this range as an extended critical regime where more than 10% of nodes exhibit $DFA_{exp} \geq 0.65$.

Next, we extended the analysis by varying global coupling (L) and local coupling (K) strength simultaneously. We created a cohort of structural-connectome-informed models ($N = 24$) and analyzed the behavior of intra- and internode level observables.

At the nodal level, we found that the DFA exponent peaks during the phase transition of the node order (Fig. 2*F*). On the K-L surface defined as the DFA exponent as a function of both control parameters, the critical region was represented by a linear critical ridge (defined as a region where average $DFA_{exp} \geq 0.6$) and reached a maximum when local coupling was slightly higher than global (Fig. 2*G*).

Internodal interaction dynamics showed a transition from near zero synchronization to almost perfect synchrony, albeit the cross-correlation between node order time series peaking during the transition period and its peak matching the critical region assessed with LRTCs (Fig. 2 *H* and *I*). Unlike the DFA exponent that was maximized when $K > L$, the cross-correlation achieved the highest values when $L > K$.

In addition to LRTCs (18), neuronal avalanches with power-law size and lifetime distributions are another key hallmark of critical-like dynamics (19). To assess avalanche dynamics in the Hierarchical Kuramoto model, we first extracted the zero phase crossing events for each node oscillator (57), then defined a neuronal avalanche as any contiguous period during which this series exceeded its median, and finally the avalanche size as the total number of events during this period (*SI Appendix*, Fig. S1*A*, (70)). To estimate proximity to criticality, we computed the κ-index that is a similarity metric between the observed cumulative distribution function (CDF) of avalanche sizes and an ideal power-law distribution with a scaling exponent of $\alpha = \frac{-3}{2}$ (Fig. 2*J*, see *SI Appendix* for details) (25, 71).

In line with studies on the branching process and spiking models (19, 72), we found that the model exhibited avalanches with power-law scaling with an exponent of $\frac{-3}{2}$ at criticality. In the subcritical phase, the avalanche size distributions decayed exponentially for large avalanches while the supercritical phase exhibited a clear characteristic scale (*SI Appendix*, Fig. S1*B*). Avalanche size distributions approached the reference power law yielding $\kappa < 1$ in the subcritical regime, $\kappa \approx 1$ near criticality, and $\kappa > 1$ in the supercritical regime (Fig. 2 *K* and *L*), which is well aligned with prior studies on avalanche dynamics in several kinds of systems, including the branching process, spiking neuronal systems, and the mean-field directed percolation universality class (20, 25, 33).

To verify robustness of the results to alterations in the internodal connectome, we employed two control models: in the first model, the SC was log-transformed to verify that rare strong connections do not bias the results. Using the second model, we tested how sparseness in a connectome affects the key observables and randomly set K% (0–10–20–30–40%) of edges to zero preserving connectome symmetry. We found these control models to be phenomenologically identical to the models based on the original connectome, with very similar phase transition from disorder to order and emergence of LRTCs at the transition (*SI Appendix*, Figs. S2 and S3).

Interaction-Specific Breakdown or Maximization of In Silico Structure–Function Coupling at Criticality. The SC is a backbone of functional relations in the brain and previous studies have shown that models initialized with the human structural connectome can reconstruct patterns of resting-state networks (31, 73). Although their primary focus was specific features of activity, such as FC, they did not investigate behavior of multiple observables at once and impact of operating point on structure–function correlations.

To analyze relationships between the model's structural architecture and oscillatory dynamics, we employed the in silico pipeline and computed the Pearson correlation coefficient between internode connection weights of a SC-informed model and observables of oscillatory dynamics. We correlated node strength (NS, average SC of a node) with node-level observables (e.g., order, DFA exponent), and internode statistics [e.g., edge strength of PLV/amplitude cross-correlation (CC)] were correlated with edge weights (Fig. 3*A*).

Investigating the structure–function coupling in the model at the individual node level, we found that node order was positively correlated with node strength, increasing slightly from the subcritical to the critical region, dipping at criticality, and then increasing sharply in the supercritical region (Fig. 3*B*). The correlation between the DFA exponent and NS, on the other hand, fluctuated around zero in the subcritical region, peaked at criticality, and became strongly negative in the supercritical zone (Fig. 3*C*). A similar phenomenon was observed on the K-L surface where DFA vs. structure correlation was maximized in the critical region (Fig. 3*C*).

At the edge level, the correlation between edge strength and CC resembled the patterns observed with the DFA exponent, peaking at criticality while remaining low in both subcritical and supercritical zones (Fig. 3*E*). The correlation between PLV and edge strength exhibited a unimodal shape, with a wide peak on the subcritical side and a drop around the critical peak (Fig. 3*D*). Unlike other observables, PLV showed higher correlation with SC in regions where global coupling was stronger than local coupling (Fig. 3*D*). Phenomenologically similar results were observed with control models computed obtained with log-transformed internode connectome and for different degrees of connectome sparsiness (*SI Appendix*, Figs. S4 and S5).

These results demonstrated that synchronization and criticality in oscillatory dynamics were associated with unique correlation regimes between structural and functional properties. In the critical regime, the correlations between edge weights and intra- or interareal synchronization decreased, whether LRTCs and cross-correlations reached their peak.

Brain Dynamics During the Resting-State Are the Most Correlated with Observables on Subcritical Side of the Extended Critical Regime. Having mapped how local and global coupling shape oscillatory dynamics in silico (Figs. 2 and 3), we next tested where in the K-L surface the model observables best match those of resting-state MEG. To answer this question we computed key observables of oscillatory dynamics for resting-state MEG data, including the weighted Phase Lag Index (wPLI), DFA exponents, and orthogonalized amplitude cross-correlation (oCC, Fig. 4*A*, see *SI Appendix* for details). For wPLI and oCC we also included in the analysis the average value across edges that belonged to the same node (node strength).

Next, we computed analogous observables for simulated data but operationalized phase synchronization with PLV instead of wPLI (Fig. 4*B*). Finally, to evaluate the model-data similarity, we estimated Pearson's correlation coefficients between observables from model nodes/edges and MEG parcels/edges corresponding to the same anatomical regions.

We first assessed the MEG similarity as a function of narrow-band data frequency. The model showed the most similar dynamics to the low-frequency activity, particularly in the theta frequency range (3 to 8 Hz) for the DFA exponent and node- and edge-level phase-synchronization (Fig. 4*C*). However, the amplitude correlation exhibited several significant peaks including at theta (4.75 Hz), alpha (12.3 Hz), and beta frequencies (28.3 Hz).

To test whether the similarities were a product of the realistic structural connectome, we computed the same model-MEG

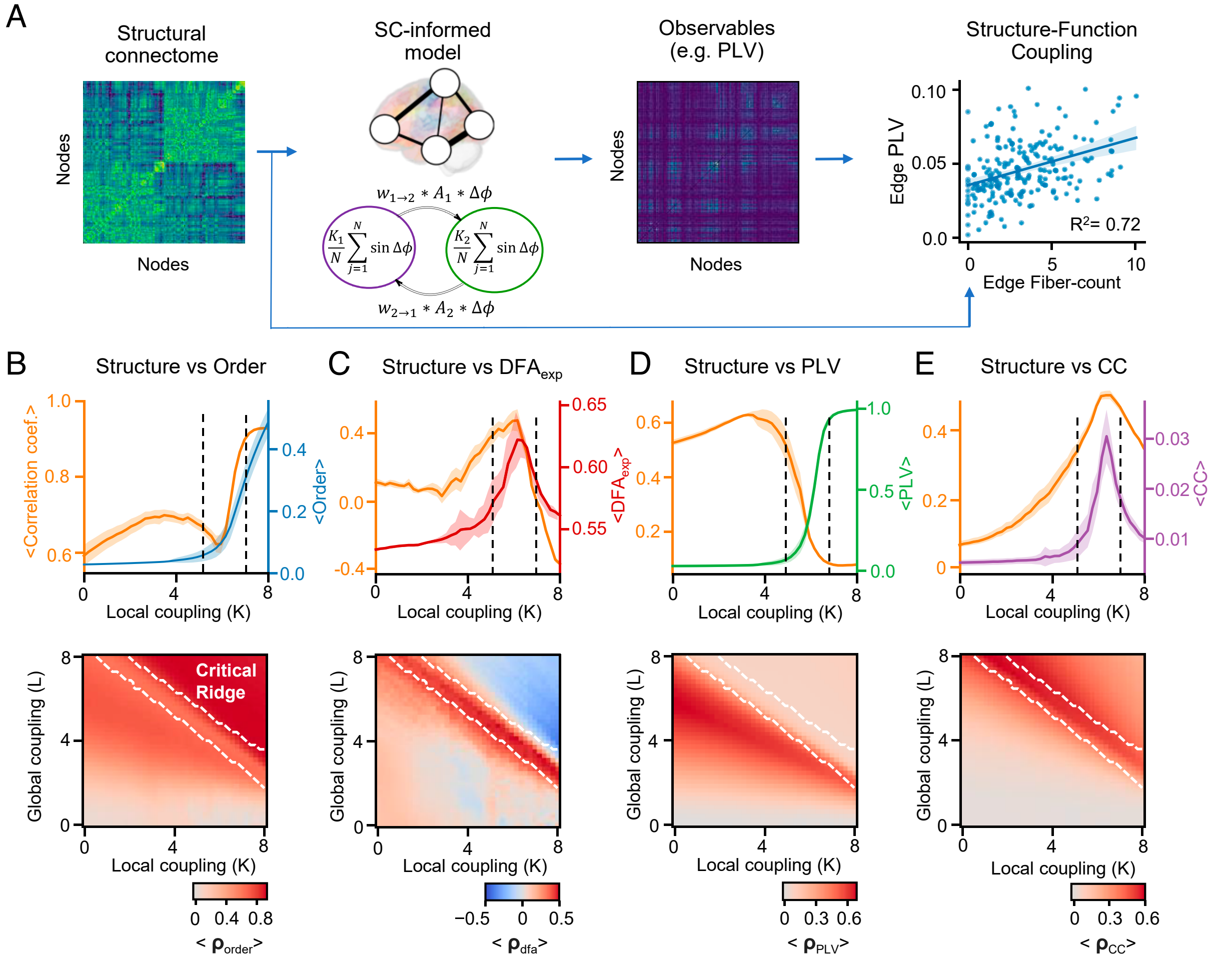

Fig. 3. Modeling reveals diverse forms of Structure–Function coupling around the phase transition. (*A*) Analysis pipeline: The SC matrix of an individual is used to construct an SC-informed Kuramoto model, where edge coupling weights are derived from the SC. The model generates time series, from which observables such as Phase Locking Value (PLV), DFA exponent (DFA_{exp}), order, and amplitude cross-correlation (CC) are computed. Structure–function coupling is quantified as the correlation between these observables and structural measures (e.g., node strength or edge fiber count). (*B*–*E*) Correlation between model order and SC node strength (*B*), DFA_{exp} and SC node strength (*C*), PLV and SC edge weight (*D*), node order cross-correlation and edge weight (*E*) as a function of local coupling strength (K). The orange line indicates Pearson correlation coefficient (ρ), other colored lines represent a model observable. Shaded areas represent CIs based on SE. On the bottom, heatmaps showing the Pearson correlation coefficient between the respective observables and structural measures (node strength or edge strength) as functions of local (K) and global (L) coupling strengths. The white contour outlines the critical ridge, defined as a region where average $DFA_{exp} \geq 0.6$, consistent with Fig. 2.

correlations for data simulated with two null models: using the shuffled structural connectome and a random uniform. For these null models, the correlations were nonsignificant (Fig. 4*C*) showing that realistic architecture of node connectivity was crucial to produce in vivo-like dynamics.

Second, we asked how the similarity between simulations and MEG behaved as a function of model control parameters. For each observable, we investigated the frequency with the highest correlation between the model and MEG data. We found that the significant correlation for all observables included in the analysis was found along the critical ridge (Fig. 4 *D*–*H*), which supports the notion that the human brain operates primarily on a subcritical side of the extended critical regime.

The Spectral Properties of Oscillatory Activity Are Shaped by the Distribution of Underlying Frequencies and Position in the Critical State Space. Traditionally, oscillations are quantified by their magnitude, often using power spectral methods. Different system properties, such as interaction delays (45) or cortical layer organization (74), have been shown to regulate the shape of the spectra and the emergence of oscillatory modes. However, the role of a system operating point remains an open question.

To replicate individual power spectral properties in the model, we aligned the oscillator frequency distribution with the shape of the recorded power spectrum (see Fig. 5*A* and *SI Appendix* for details). We first verified whether a model using a data-driven frequency distribution would exhibit critical-like dynamics. Indeed, we found that initializing the model with a nonparametric distribution of oscillator frequencies produced critical-like dynamics, with LRTCs emerging at the phase transition while preserving multifrequency activity (see *SI Appendix*, Fig. S6 *A* and *B*).

Next, to assess the similarity between the real and simulated data, we computed PSD of the simulated and MEG data using the Welch method and estimated the Pearson correlation coefficient between them. In addition, we estimated the model frequency shift calculated by the absolute distance between the alpha peak in the model and the MEG spectra.

Regions with low intranodal and high internodal coupling in the subcritical regime showed weak, almost absent peaks in the power spectrum. As the model approached the critical regime, oscillatory peaks gradually emerged and became dominated by the alpha band, closely matching those observed in the real MEG data (Fig. 5*B*). In the supercritical regime, a pronounced alpha peak appeared together with a slight spectral drift toward the weighted

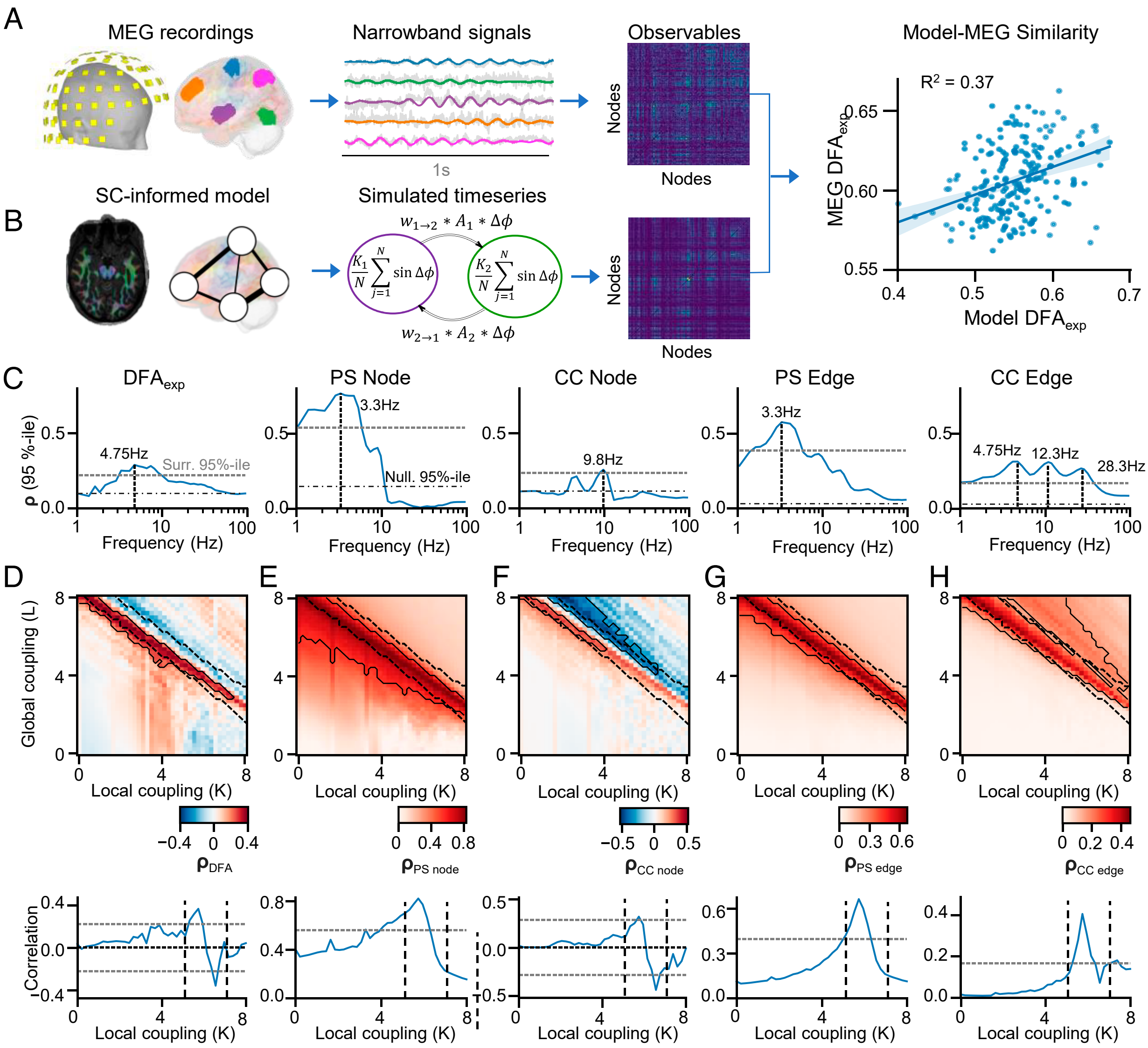

Fig. 4. The model observables on the subcritical side of the extended critical regime most closely match the patterns seen in human MEG recordings. (*A*) MEG analysis pipeline: MEG recordings are source-modeled to derive parcel-level time series, filtered into narrowband signals (e.g., using Morlet wavelets), and used to compute observables such as phase synchronization matrices. (*B*) Modeling pipeline: using the SC-informed Kuramoto model, we simulated time series and derived observables—such as phase synchrony (PLV/wPLI) and LRTCs (DFA exponent)—comparable to those obtained from MEG data. (*C*) The 95th percentile of the Pearson correlation coefficient across the K-L surface between MEG and model observables as a function of frequency. The dashed horizontal line indicates the statistical significance threshold determined via spin-permutation tests. The dash-dotted line indicates the 95th percentile of correlations in null model obtained by shuffling the structural connectome. The vertical dashed line highlights the frequency at which the correlation peaks. (*D*–*H*) Correlation maps and K-L surface slices for observables at the peak frequency identified in *C*. The Pearson correlation coefficient between simulated and MEG-derived DFA exponent (*D*), average phase-synchronization of a node (*E*), average cross-correlation of a node (*F*, edge phase synchrony (*G*), and edge cross-correlation (*H*) as a function of local (K) and global (L) coupling coefficients for frequency with maximum 95th percentile (*C*). Black dashed contours in the heatmaps indicate regions with statistically significant correlations ($P < 0.01$) based on spin-permutation tests. Black dashed contours delineate the critical ridge, defined as a region where average $DFA_{exp} \geq 0.6$, consistent with Figs. 2 and 3. The line plots at the bottom represent a slice of the K-L surface for the same $L = 4$.

average of alpha (9.8 Hz) and beta (19.5 Hz) frequencies, yielding a weighted mean of 12.85 Hz (Fig. 5*E*).

Quantifying the similarity between the model and the MEG-derived power spectrum, we found that the highest correlation was achieved on the subcritical side of the extended critical regime, with high local and low global coupling strength, and decayed after the critical ridge (Fig. 5 *C* and *D*). To test whether data-driven initialization of oscillator frequencies improves the model-data similarity, we compared it to the null-model where oscillator frequencies were drawn from the Gaussian distribution with mean value set to the highest peak in the PSD of each node. We found that although such a model can reproduce the primary peak in the alpha peak frequency, the secondary peak in the beta band is absent (*SI Appendix*, Fig. S6*C*). Quantitatively, among the top-10% model parameters selected by correlation, model-data similarity is lower with the Gaussian initialization (mean 0.81 vs. 0.92; *SI Appendix*, Fig. S6*D*).

Discussion

We present here a Hierarchical Kuramoto model that captures concurrently both functional-connectivity and brain-criticality phenomena and enables linking them across meso- and macroscopic scales of brain synchronization dynamics. Synchronization and criticality are interconnected in emergent brain activity so that their in vivo interindividual and -regional variability is

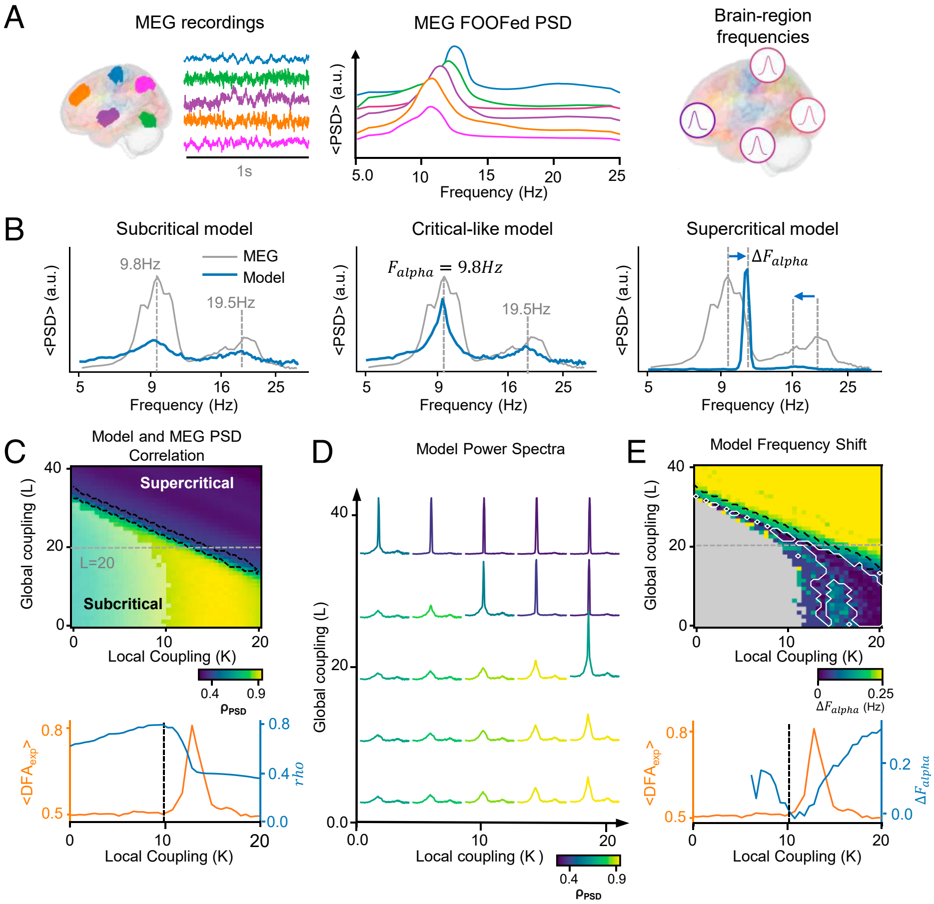

Fig. 5. Critical-like state supports multifrequency spectral properties. (*A*) Oscillator frequency distribution derived from parcel-level power spectral density (PSD) of real MEG recordings (*Left* panel), with the $1/f$ component subtracted (*Middle* panel) and are individually set for mode node that corresponds a brain area (*Right* panel). (*B*) Average PSD across model nodes (blue) compared with MEG-derived PSD (gray) for three regimes: subcritical, critical, and supercritical. Dashed vertical lines indicate the alpha (~9.8 Hz) and beta (~19.5 Hz) frequency peaks. The critical model aligns closely with MEG-derived PSD, while subcritical and supercritical regimes deviate. (*C*) Pearson correlation coefficient between MEG-derived and simulated PSD as a function of local (K) and global (L) coupling strengths (*Upper* panel). The black contour highlights the critical ridge defined as a region, where average $DFA_{exp} \geq 0.6$. The semitransparent area indicates regions without significant spectral peaks. *Bottom* panel: Correlation coefficient (blue) and average DFA_{exp} (red) as functions of local coupling (K) for a fixed global coupling ($L = 20$). (*D*) Model PSD for different combinations of local (K) and global (L) coupling strengths, color-coded by their correlation with MEG-derived PSD, as shown in *C*. Simulated spectra with critical-like dynamics exhibit the most realistic multipeak structure. (*E*) Difference between simulated and MEG alpha peak frequencies (ΔF_{alpha}) averaged across model nodes as a function of control parameters. The white contour highlights regions with significant alignment of alpha peaks. *Bottom* panel: ΔF_{alpha} (blue) and average DFA_{exp} (red) as functions of local coupling (K), indicating the region of optimal alpha frequency alignment with critical-like dynamics.

likely driven by variability in the underlying individual and local operating points (32). Thus, a generative model that integrates these two aspects is essential for studying brain dynamics and developing experimentally testable, mechanistic predictions.

We assessed the plausibility of the model with three lines of inquiries. First, we found that the structure–function coupling in the model was both strongly dependent on the operating point in an opposing manner for phase synchronization and amplitude dynamics. Next, we tested the anatomical similarity between the model and resting-state MEG observables and found moderate to large correlations that peaked in the subcritical-side of the model's extended critical regime across all observables. Finally, initializing oscillator frequencies from the MEG-derived PSD enabled the model to reproduce concurrent multifrequency oscillations that peaked at criticality and most closely matched MEG resting-state dynamics on the subcritical side of the extended critical regime. These findings thus establish a modeling framework for assessing how local and global operating points regulate emergent brain dynamics, opening avenues for mechanistic understanding of macroscale brain activity.

Concurrent Modeling of Local and Global Critical Synchronization Dynamics. Brain dynamics arise across scales, from microcircuits to macroscopic populations. Therefore, concurrent consideration of local and interareal dynamics is essential for modeling brain activity. Hierarchical methods have recently gained traction in modeling neuronal activity, where they have been used to combine models at different scales (75). For example, they can integrate both spiking and mean-field activity simultaneously to accurately predict the effects of deep brain stimulation (76) or simulate local and network-level interactions (77).

Building on these advances, our framework adapts the Kuramoto approach to model synchronization directly, rather than through modeling the putative underlying biophysical mechanisms. Unlike neural-mass models or oscillators with intrinsic amplitude dynamics (e.g., Hopf or Stuart-Landau), where amplitude reflects the distance from equilibrium, expressing the node "amplitude" via the Kuramoto order parameter provides a direct and explicit measure of local synchronization. This is essential in the context of electrophysiological neuroimaging, including MEG and EEG, where the local signal amplitude is primarily determined by local synchronization (1, 63–65).

Extending a two-level hierarchical implementation of the Kuramoto model to the whole-brain scale, we found that simultaneous modeling of local and interareal synchronization dynamics reveals a multiscale transition from an asynchronous to a synchronized phase in both node order and interareal phase synchrony. With high-resolution multichannel data such as modern electrophysiological or imaging recordings that can capture massive amounts of individual neuronal signals, neuronal microcircuits, and larger meso- and macroscale population activities concurrently, this framework could be extended to three or more hierarchical levels, linking microcircuit, local, and large-scale network dynamics.

In biological networks, transitions from order to disorder are governed by the balance of excitation and inhibition, which controls the emergence and stability of synchronization. E/I balance is thus thought to be a key control parameter regulating synchronization in in vivo neuronal systems (24, 26, 71). While the Kuramoto model does not express synaptic neuronal interactions, such as the spiking and postsynaptic dynamics as in the CROS model (25, 52), it models the synchronization phenomenon itself. Indeed, both frameworks produce systems that exhibit a phase transition between disordered (asynchronous) and ordered (synchronized) states, with critical dynamics emerging at this transition. In addition, the emergence of amplitude cross-correlation peaked at criticality in both CROS (51) and Hierarchical Kuramoto frameworks show convergent discovery of unmodeled, emergent phenomena in both modeling approaches. Thus, although the coupling mechanisms and control parameters are distinct, spiking neuron and Kuramoto systems exhibit homologous dynamics and phenomenology across the phase transition.

At the node level, the phase transition was associated with emergence of long-range temporal correlations (LRTCs) that evidence local critical-like dynamics (18, 33, 78). In interareal coupling, this phase transition in synchronization was associated with maximized node-order correlations, i.e., amplitude correlations of the local oscillations that largely reflect interareal coupling of local synchronization fluctuations in experimental data. Together with phase synchrony (3, 4, 10), amplitude correlations are a key mode of "functional connectivity" in human brain dynamics both at macro- (79) and mesoscopic levels (2).

Although the structural phase-synchronization and amplitude-correlation networks show considerable anatomical overlap (80), their underlying mechanisms may be distinct. Recent in vivo studies suggest that differences in phase and amplitude coupling can be explained by burst dynamics (81) or from regional variations in neurotransmitter density (82). Here, we extend these findings by showing that the two measures depend differently on the operating point: phase synchrony increases monotonically, whereas amplitude correlations follow a quadratic-like relationship peaking at criticality.

Unique Profiles of Structure–Function Coupling Across the Critical Phase Transition. Large-scale brain activity is shaped and constrained by interareal structural connectivity (SC) defined especially by white-matter axonal projections (83). Both fMRI and MEG studies have shown that functional connectivity networks are correlated with the SC networks but with notable anatomical variability in this structure–function coupling (SFC) (84–86). The relationship of SFC with brain criticality and the operating point of neuronal systems has, however, remained controversial. On one hand, computational modeling suggests that SC and FC decouple at criticality due to the emergence of correlations (functional connectivity) between areas that are not directly structurally connected (30). On the other hand, comparisons between modeled and fMRI resting-state networks, suggest that FC emerges directly from SC at criticality (73, 87). To address this conundrum, we assessed the anatomical similarity between SC and oscillatory dynamics as a function of the model's operating point. Synchronization was strongly correlated with SC in the subcritical regime, but this relationship broke down at criticality as a result of emergent indirect correlations. Thus while SC constrains phase synchronization in the subcritical phase, even nodes with weak SC can synchronize via higher-order interactions at criticality. However, in contrast with phase synchronization, both the local DFA exponents and interareal amplitude correlations exhibited the strongest correlations with SC at criticality.

SFC has important implications for the controllability of the brain as a complex system. Differences in network structure suggest different roles in controlling brain states. Highly connected hub regions often have the strongest influence on network dynamics (88, 89). However, rather than operating to a single regime of dynamics, neuronal systems exhibit multiple distinct dynamical states (37, 90). Linear controllability has been assessed in a series of studies and approaches to brain modeling (88, 91, 92). Our findings show the emergence of nonlinear dynamics and second-order interactions at criticality, suggesting that in the critical regime linear control might be less effective than in the subcritical state.

Model Dynamics Match Meg Data in the Subcritical Side of an Extended Critical Regime. The "critical brain" hypothesis suggests that the brain operates at intermediate levels of synchronization near a phase transition between order and disorder (17, 20, 69) where power-law temporal correlations (18, 32, 33) and neuronal avalanches (33, 70, 93) emerge.

Despite recent advances in approaches to measure the distance to criticality, observing the operating point of human brains in vivo has remained a central unresolved objective in the field (32, 34). Comparing computational model and experimental data is a well-established way to understand the effects of structure and mechanisms on emergent dynamics in complex systems (39). Human whole-brain scale modeling has shown that models tuned to criticality (31, 73), those operating at maximum metastability (45, 94), as well as the models based on Hopf oscillators achieve the greatest similarity with experimentally observed functional connectivity in fMRI (55) and MEG data (68). In addition, the CROS model tuned to criticality was also able to reproduce the distribution of DFA exponents found in MEG data (52). in vivo studies support these results and it was found that avalanche size distribution of spiking activity in rats is the most similar to models tuned to criticality (95), the anesthesia effect on criticality in rats (96), and the link between criticality in brain and behavior dynamics (18, 97, 98).

Earlier studies have not assessed the model-experiment correlations simultaneously for FC and criticality properties while both are dependent on the operating point. To address this, we compared the topographies of model observables with those in resting-state MEG. We were able to reproduce the observed patterns of MEG activity in controlled in-silico manipulations, changing to model control parameters while preserving all other system properties fixed (such as SC architecture). Throughout all studied observables, the greatest similarity between model and experimental observables was found systematically on the subcritical side of an extended critical regime. These findings thus extend the prior studies with a line of evidence for the notion that most human individuals during resting-state operate on the subcritical side rather than at the peak or in the supercritical side of the critical regime. Although the model-MEG comparisons here leverage a correlative approach and thus do not provide causal inference about the state or operating point of human brains in vivo, the in silico modeling shows a causal association of control parameters, operating point, and emergent dynamics, which suggests that also in vivo these a mechanistic link between these constructs and observables.

Scale-free statistics are not unique to critical phase transitions. Alternative mechanisms—including random-walk-like processes with memory, nonstationarity, and mixtures of states—can generate heavy-tailed or $\frac{1}{f^{\beta}}$ patterns, and avalanche exponents can be sensitive to thresholding, binning, and subsampling (70, 99–101). To mitigate these challenges, it is essential to extend the analytical approaches to include multiple observables of critical-like dynamics. Several lines of evidence in the present and prior studies support the notion of brains operating largely on the subcritical side of an extended critical regime (32, 102). In the present study, this is implied by several conditions: multiple independent observables (node-level LRTCs, interareal phase synchrony) showed the expected control-parameter-dependent changes along the K-L surface where phase synchrony and node order increased monotonically from the region with low control parameters to high while the DFA exponents peaked at the phase transition from low to high order. The peak in DFA-based LRTCs, which indicates critical-like dynamics, was colocalized with $\kappa = 1$, which corresponds to critical avalanche dynamics, as well as with the peak in amplitude correlations reflecting emergent second-order correlations. Structure-based controls (sparsified and shuffled/uniform null models) disrupted MEG-model similarity while still exhibiting phenomenologically similar behavior with, e.g., critical-like dynamics and structure–function coupling. These results together support the notion of the Hierarchical Kuramoto model exhibiting critical dynamics where the operating point is governed by the control parameters of the model.

Excitation–inhibition balance, or excitability, as the primary control parameter for criticality in neuronal systems, exhibits continuous infraslow (0.01 to 0.1 Hz) fluctuations both during sleep (103) and awake resting (104, 105) as well as distinct differences between cognitive states (71). Modeling carried out in the present study was based on time-invariant control parameters, which yields insight into the specific nature of emergent dynamics along the control parameter axes. In addition, the in vivo variability in excitability thus suggests that the operating point of brains or brain systems fluctuates according to these control parameter variations.

Operating Point Shapes Multifrequency Oscillatory Dynamics. The human brain exhibits oscillations at multiple frequencies concurrently (5, 106, 107) which are typically operationalized as peaks in the power spectrum (108). Prior studies have indicated that specific aspects of the power spectrum are influenced by factors such as delayed interactions (45), or cortical layers' organization (74). However, typically models with only a single central frequency have been studied and the role of operating point in a system with several concurrent oscillation frequencies has remained unknown.

Our results show that the spectral properties are defined by both the distribution of underlying oscillators' frequencies and a system position in the critical state space. The shape of the PSD was primarily dictated by the frequency distribution of the oscillators. When this distribution aligned with the shape of the MEG-derived PSD, the model was able to reproduce key properties such as location of spectral peaks. The operating point regulates the emergence of multiple peaks, from an almost complete absence of oscillations in the subcritical region to a singular frequency in the supercritical regime. Notably, in the subcritical-to-critical regime, the model preserves a multimodal spectrum and achieves the highest similarity with PSD as observed in MEG experiments. Following these results, we propose that operating in this regime provides sufficient local synchronization to produce sustained oscillations, as indicated by significant peaks in the power spectrum, while also preserving the necessary variability in activity to support multifrequency dynamics.

Criticality is a rapidly emerging framework in brain research that posits an operating point governing the variability in neuronal dynamics. However, the effect of this operating point on functional properties has remained unclear. In this work, we introduced a generative hierarchical framework for modeling critical-like dynamics that explicitly captures both local and interareal synchronization. Our model exhibits emergent multiscale dynamics that replicate several features of critical meso- and macroscale brain activity observed in electrophysiological recordings. Importantly, the model captures key sources of biological heterogeneity that shape large-scale brain dynamics. Variability in structural connectivity naturally gives rise to regional differences in functional coupling, consistent with the empirically observed structure–function relationship. Likewise, the use of empirically derived oscillator frequency distributions explains the emergence of multiple spectral peaks in the simulated power spectra, mirroring those observed in MEG recordings.

The results demonstrated the causal effect of the operating point on structure–function coupling and spectral properties of multifrequency oscillations in the model. We believe this approach highlights the importance of critical-like state in the complex dynamics and opens avenues for whole-brain modeling to investigate the role of control parameters on brain activity to guide personalized treatment strategies, such as targeted brain stimulation.

Materials and Methods

Hierarchical Kuramoto Model. We introduce a hierarchical extension of the Kuramoto model with multiple nodes comprising multiple locally coupled oscillators, analogously to the analysis of electrophysiological recordings, where each electrode or cortical parcel represents a large number of locally interacting neurons. The behavior of individual oscillators within a node is governed by three terms: $\frac{\delta \phi_i^n}{\delta t} = Natural + Internal + External + Noise,$ where $Natural = w_i^n$ represents a frequency of the i-th oscillator in the n-th node and ϕ_i^n is the oscillator phase,

$Internal = \frac{K_n}{N} \sum_{j=1}^{N} sin(\phi_j^n - \phi_i^n).$

Representing dynamics internal for each node, where K_n is the local coupling parameter of the n-th node and N is the total number of oscillators within the node. In this context, the phase of each oscillator is shifted toward the average phase of oscillators within a node,

$External = \sum_{j=1}^{k} L^{n,j} * W^{n,j} * sin(\Phi^j - \phi_i^n) * R^j.$

Representing interactions external to a node, where $L^{n,j}$ is the coupling coefficient between the n-th and j-th nodes (global control parameter), $W^{n,j}$ is the SC between the n-th and j-th nodes, Φ^j is the cyclic average of the phases of the j-th node defined as $\Phi^j = arg(\frac{1}{N} \sum_{q=1}^{N} e^{i\phi_q^j})$ and R^j is the order (complex modulus) of the j-th node. In this context, the phase of each oscillator is compared to the average phase of other nodes and weighted by a target node order and edge strength while within-node oscillators are connected in all-to-all fashion with the weight equal to K.

$Noise = \eta_i^n$ is the white noise for the i-th oscillator in the n-th node.

The detailed explanation and visualization of model parameters and their values for each experiment are shown in *SI Appendix*, Fig. S8 and Table S1.

Data, Materials, and Software Availability. The simulation and the model code are deposited in the publicly available repository (https://github.com/palvalab/hierarchical_kuramoto_zero) (109) include scripts needed to run the computational experiments mentioned in the study. The repository also contains a tutorial for the model usage and basic analysis. The MEG and DWI datasets generated and analyzed in the current study are not publicly available due to patient privacy limitations set forth in the Ethical Committee approval along with General Data Protection Regulation (GDPR) constraints. The full study protocol was approved by the HUS ethical committee (HUS/3042/2021 and the Finnish Medicines Agency (FIMEA/2022/002976), written informed consent was obtained from each participant prior to the experiment, and all research was carried out according to the Declaration of Helsinki. The details of MEG and DWI data recording processing can be found in *SI Appendix*.

ACKNOWLEDGMENTS. We thank Sheng Wang, Felix Siebenhühner, Joonas J. Juvonen, Jussi Häkkänen and Joona Repo for their feedback on the study and manuscript. We also thank professor Guido Nolte on helpful comments on an earlier version of the manuscript. The simulations have been done on the LUMI and TRITON supercomputer. This study was supported by the Academy of Finland (J.M.P., Project No. 296304), by the Juselius Foundation (S.P. and J.M.P. Project No. 240156) and by Business Finland (J.M.P. project number: 1670/31/2024).

Author affiliations: [a]Department of Neuroscience and Biomedical Engineering, Aalto University, Espoo FI-00076, Finland; [b]Neuroscience Center, Helsinki Institute of Life Science, University of Helsinki, Helsinki FI-00014, Finland; [c]Division of Psychology, VISE, Faculty of Education and Psychology, University of Oulu, Oulu G12 8QB, Finland; [d]BioMag Laboratory, Uusimaa Hospital Diagnostic Center, Helsinki FI-90014,Finland; and [e]School of Psychology and Neuroscience, University of Glasgow, Glasgow FI-00029, United Kingdom

1. G. Buzsáki, C. A. Anastassiou, C. Koch, The origin of extracellular fields and currents–EEG, ECOG, LFP and spikes. *Nat. Rev. Neurosci.* **13**, 407–420 (2012).
2. G. Arnulfo, J. Hirvonen, L. Nobili, S. Palva, J. M. Palva, Phase and amplitude correlations in resting-state activity in human stereotactical EEG recordings. *NeuroImage* **112**, 114–127 (2015).
3. G. Arnulfo *et al.*, Long-range phase synchronization of high-frequency oscillations in human cortex. *Nat. Commun.* **11**, 5363 (2020).
4. S. Palva, J. M. Palva, Discovering oscillatory interaction networks with M/EEG: Challenges and breakthroughs. *Trends Cogn. Sci.* **16**, 219–230 (2012).
5. J. M. Palva, S. Palva, K. Kaila, Phase synchrony among neuronal oscillations in the human cortex. *J. Neurosci.* **25**, 3962–3972 (2005).
6. E. Glerean, J. Salmi, J. M. Lahnakoski, I. P. Jääskeläinen, M. Sams, Functional magnetic resonance imaging phase synchronization as a measure of dynamic functional connectivity. *Brain Connectivity* **2**, 91–101 (2012).
7. P. Fries, Rhythms for cognition: Communication through coherence. *Neuron* **88**, 220–235 (2015).
8. M. Vinck *et al.*, Principles of large-scale neural interactions. *Neuron* **111**, 987–1002 (2023).
9. M. Schneider *et al.*, A mechanism for inter-areal coherence through communication based on connectivity and oscillatory power. *Neuron* **109**, 4050–4067.e12 (2021).
10. J. M. Palva, S. Monto, S. Kulashekhar, S. Palva, Neuronal synchrony reveals working memory networks and predicts individual memory capacity. *Proc. Natl. Acad. Sci. U.S.A.* **107**, 7580–7585 (2010).
11. H. Haque, M. Lobier, J. M. Palva, S. Palva, Neuronal correlates of full and partial visual conscious perception. *Conscious. Cogn.* **78**, 102863 (2020).
12. F. Siebenhühner, S. H. Wang, J. M. Palva, S. Palva, Cross-frequency synchronization connects networks of fast and slow oscillations during visual working memory maintenance. *eLife* **5**, e13451 (2016).
13. S. H. Wang *et al.*, Neuronal synchrony and critical bistability: Mechanistic biomarkers for localizing the epileptogenic network. *Epilepsia* **65**, 2041–2053 (2024).
14. L. I. Boon *et al.*, A systematic review of meg-based studies in Parkinson's disease: The motor system and beyond. *Hum. Brain Mapp.* **40**, 2827–2848 (2019).
15. R. H. Kaiser, J. R. Andrews-Hanna, T. D. Wager, D. A. Pizzagalli, Large-scale network dysfunction in major depressive disorder: A meta-analysis of resting-state functional connectivity. *JAMA Psychiat.* **72**, 603 (2015).
16. S. Palva, S. Monto, J. M. Palva, Graph properties of synchronized cortical networks during visual working memory maintenance. *NeuroImage* **49**, 3257–3268 (2010).
17. D. R. Chialvo, Emergent complex neural dynamics. *Nat. Phys.* **6**, 744–750 (2010).
18. K. Linkenkaer-Hansen, V. V. Nikouline, J. M. Palva, R. J. Ilmoniemi, Long-range temporal correlations and scaling behavior in human brain oscillations. *J. Neurosci.* **21**, 1370–1377 (2001).
19. J. M. Beggs, D. Plenz, Neuronal avalanches in neocortical circuits. *J. Neurosci.* **23**, 11167–11177 (2003).
20. W. L. Shew, D. Plenz, The functional benefits of criticality in the cortex. *Neuroscientist* **19**, 88–100 (2012).
21. N. Lotfi *et al.*, Statistical complexity is maximized close to criticality in cortical dynamics. *Phys. Rev. E* **103**, 012415 (2021).
22. O. Kinouchi, M. Copelli, Optimal dynamical range of excitable networks at criticality. *Nat. Phys.* **2**, 348–351 (2006).
23. V. Zimmern, Why brain criticality is clinically relevant: A scoping review. *Front. Neural Circuits* **14**, 54 (2020).
24. J. M. Beggs, The criticality hypothesis: how local cortical networks might optimize information processing. *Philos. Trans. R. Soc. A, Math. Phys. Eng. Sci.* **366**, 329–343 (2007).
25. S. S. Poil, R. Hardstone, H. D. Mansvelder, K. Linkenkaer-Hansen, Critical-state dynamics of avalanches and oscillations jointly emerge from balanced excitation/inhibition in neuronal networks. *J. Neurosci.* **32**, 9817–9823 (2012).
26. J. Simola *et al.*, Genetic polymorphisms in COMT and BDNF influence synchronization dynamics of human neuronal oscillations. *iScience* **25**, 104985 (2022).
27. J. M. Shine *et al.*, Computational models link cellular mechanisms of neuromodulation to large-scale neural dynamics. *Nat. Neurosci.* **24**, 765–776 (2021).
28. J. M. Shine, Neuromodulatory control of complex adaptive dynamics in the brain. *Interface Focus* **13**, 20220079 (2023).
29. R. E. Brown, J. T. McKenna, Turning a negative into a positive: Ascending GABAergic control of cortical activation and arousal. *Front. Neurol.* **6**, 135 (2015).
30. J. M. Beggs, N. Timme, Being critical of criticality in the brain. *Front. Physiol.* **3**, 163 (2012).
31. M. Rubinov, O. Sporns, J. P. Thivierge, M. Breakspear, Neurobiologically realistic determinants of self-organized criticality in networks of spiking neurons. *PLoS Comput. Biol.* **7**, e1002038 (2011).
32. M. Fuscà *et al.*, Brain criticality predicts individual levels of inter-areal synchronization in human electrophysiological data. *Nat. Commun.* **14**, 4736 (2023).
33. J. M. Palva *et al.*, Neuronal long-range temporal correlations and avalanche dynamics are correlated with behavioral scaling laws. *Proc. Natl. Acad. Sci. U.S.A.* **110**, 3585–3590 (2013).
34. K. B. Hengen, W. L. Shew, Is criticality a unified setpoint of brain function? *Neuron* **113**, 2582–2598.e2 (2025).
35. H. Bruining *et al.*, Measurement of excitation-inhibition ratio in autism spectrum disorder using critical brain dynamics. *Sci. Rep.* **10**, 9195 (2020).
36. P. Ritter, M. Schirner, A. R. McIntosh, V. K. Jirsa, The virtual brain integrates computational modeling and multimodal neuroimaging. *Brain Connectivity* **3**, 121–145 (2013).
37. G. Deco, V. K. Jirsa, P. A. Robinson, M. Breakspear, K. Friston, The dynamic brain: From spiking neurons to neural masses and cortical fields. *PLoS Comput. Biol.* **4**, e1000092 (2008).
38. M. Breakspear, S. Heitmann, A. Daffertshofer, Generative models of cortical oscillations: Neurobiological implications of the Kuramoto model. *Front. Hum. Neurosci.* **4**, 190 (2010).
39. M. Breakspear, Dynamic models of large-scale brain activity. *Nat. Neurosci.* **20**, 340–352 (2017).
40. G. Deco *et al.*, Resting-state functional connectivity emerges from structurally and dynamically shaped slow linear fluctuations. *J. Neurosci.* **33**, 11239–11252 (2013).
41. N. Williams *et al.*, The influence of inter-regional delays in generating large-scale brain networks of phase synchronization. *NeuroImage* **279**, 120318 (2023).
42. A. Byrne, R. D. O'Dea, M. Forrester, J. Ross, S. Coombes, Next-generation neural mass and field modeling. *J. Neurophysiol.* **123**, 726–742 (2020).
43. M. L. Kringelbach, A. R. McIntosh, P. Ritter, V. K. Jirsa, G. Deco, The rediscovery of slowness: Exploring the timing of cognition. *Trends Cogn. Sci.* **19**, 616–628 (2015).
44. P. Tewarie *et al.*, Tracking dynamic brain networks using high temporal resolution meg measures of functional connectivity. *NeuroImage* **200**, 38–50 (2019).
45. J. Cabral *et al.*, Metastable oscillatory modes emerge from synchronization in the brain spacetime connectome. *Commun. Phys.* **5**, 184 (2022).
46. G. Deco *et al.*, Awakening: Predicting external stimulation to force transitions between different brain states. *Proc. Natl. Acad. Sci. U.S.A.* **116**, 18088–18097 (2019).
47. J. Cabral, E. Hugues, O. Sporns, G. Deco, Role of local network oscillations in resting-state functional connectivity. *NeuroImage* **57**, 130–139 (2011).
48. J. P. Hobbs, J. L. Smith, J. M. Beggs, Aberrant neuronal avalanches in cortical tissue removed from juvenile epilepsy patients. *J. Clin. Neurophysiol.* **27**, 380–386 (2010).
49. Y. Liu, K. A. Dahmen, Unexpected universality in static and dynamic avalanches. *Phys. Rev. E* **79**, 061124 (2009).
50. A. Levina, J. M. Herrmann, T. Geisel, Dynamical synapses causing self-organized criticality in neural networks. *Nat. Phys.* **3**, 857–860 (2007).
51. A. E. Avramiea, A. Masood, H. D. Mansvelder, K. Linkenkaer-Hansen, Long-range amplitude coupling is optimized for brain networks that function at criticality. *J. Neurosci.* **42**, 2221–2233 (2022).
52. L. Dalla Porta, M. Copelli, Modeling neuronal avalanches and long-range temporal correlations at the emergence of collective oscillations: Continuously varying exponents mimic M/EEG results. *PLoS Comput. Biol.* **15**, e1006924 (2019).
53. G. Deco, V. K. Jirsa, A. R. McIntosh, Emerging concepts for the dynamical organization of resting-state activity in the brain. *Nat. Rev. Neurosci.* **12**, 43–56 (2010).
54. M. J. Aburn, C. A. Holmes, J. A. Roberts, T. W. Boonstra, M. Breakspear, Critical fluctuations in cortical models near instability. *Front. Physiol.* **3**, 331 (2012).
55. G. Deco, M. L. Kringelbach, V. K. Jirsa, P. Ritter, The dynamics of resting fluctuations in the brain: Metastability and its dynamical cortical core. *Sci. Rep.* **7**, 3095 (2017).
56. Y. Kuramoto, International symposium on mathematical problems in theoretical physics. *Lect. Notes Phys.* **30**, 420 (1975).
57. V. Buendía, P. Villegas, R. Burioni, M. A. Muñoz, Hybrid-type synchronization transitions: Where incipient oscillations, scale-free avalanches, and bistability live together. *Phys. Rev. Res.* **3**, 023224 (2021).

58. D. P. Koller, M. Schirner, P. Ritter, Human connectome topology directs cortical traveling waves and shapes frequency gradients. *Nat. Commun.* **15**, 3570 (2024).
59. A. Escrichs *et al*., Whole-brain turbulent dynamics predict responsiveness to pharmacological treatment in major depressive disorder. *Mol. Psychiatry* **30**, 1069–1079 (2024).
60. S. H. Wang *et al*., Critical-like brain dynamics in a continuum from second- to first-order phase transition. *J. Neurosci.* **43**, 7642–7656 (2023).
61. S. Kuroki, K. Mizuseki, Excitation-inhibition balance controls synchronization in a simple model of coupled phase oscillators. *Neural Comput.* **37**, 1353–1372 (2025).
62. F. Siebenhühner *et al*., Genuine cross-frequency coupling networks in human resting-state electrophysiological recordings. *PLoS Biol.* **18**, e3000685 (2020).
63. M. Hämäläinen, R. Hari, R. J. Ilmoniemi, J. Knuutila, O. V. Lounasmaa, Magnetoencephalography—Theory, instrumentation, and applications to noninvasive studies of the working human brain. *Rev. Mod. Phys.* **65**, 413–497 (1993).
64. R. Hari, R. Salmelin, Magnetoencephalography: From squids to neuroscience. *NeuroImage* **61**, 386–396 (2012).
65. J. Gross, Magnetoencephalography in cognitive neuroscience: A primer. *Neuron* **104**, 189–204 (2019).
66. J. Cabral *et al*., Exploring mechanisms of spontaneous functional connectivity in MEG: How delayed network interactions lead to structured amplitude envelopes of band-pass filtered oscillations. *NeuroImage* **90**, 423–435 (2014).
67. S. Petkoski, J. M. Palva, V. K. Jirsa, Phase-lags in large scale brain synchronization: Methodological considerations and in-silico analysis. *PLoS Comput. Biol.* **14**, e1006160 (2018).
68. F. Siebenhühner *et al*., Spectral patterns of meg oscillatory coupling emerge from meta-stable dynamics with small coupling delays. bioRxiv [Preprint] (2025). https://doi.org/10.1101/2025.08.18.670813 (Acccesed 3 September 2025).
69. L. Cocchi, L. L. Gollo, A. Zalesky, M. Breakspear, Criticality in the brain: A synthesis of neurobiology, models and cognition. *Prog. Neurobiol.* **158**, 132–152 (2017).
70. A. Zhigalov, G. Arnulfo, L. Nobili, S. Palva, J. M. Palva, Relationship of fast- and slow-timescale neuronal dynamics in human MEG and SEEG. *J. Neurosci.* **35**, 5385–5396 (2015).
71. W. L. Shew, H. Yang, T. Petermann, R. Roy, D. Plenz, Neuronal avalanches imply maximum dynamic range in cortical networks at criticality. *J. Neurosci.* **29**, 15595–15600 (2009).
72. C. W. Eurich, J. M. Herrmann, U. A. Ernst, Finite-size effects of avalanche dynamics. *Phys. Rev. E* **66**, 066137 (2002).
73. A. Haimovici, E. Tagliazucchi, P. Balenzuela, D. R. Chialvo, Brain organization into resting state networks emerges at criticality on a model of the human connectome. *Phys. Rev. Lett.* **110**, 178101 (2013).
74. R. Sanchez-Todo *et al*., A physical neural mass model framework for the analysis of oscillatory generators from laminar electrophysiological recordings. *NeuroImage* **270**, 119938 (2023).
75. E. D'Angelo, V. Jirsa, The quest for multiscale brain modeling. *Trends Neurosci.* **45**, 777–790 (2022).
76. J. M. Meier *et al*., Virtual deep brain stimulation: Multiscale co-simulation of a spiking basal ganglia model and a whole-brain mean-field model with the virtual brain. *Exp. Neurol.* **354**, 114111 (2022).
77. H. E. Wang *et al*., Virtual brain twins: From basic neuroscience to clinical use. *Natl. Sci. Rev.* **11**, nwae079 (2024).
78. R. Hardstone *et al*., Detrended fluctuation analysis: A scale-free view on neuronal oscillations. *Front. Physiol.* **3**, 450 (2012).
79. M. J. Brookes *et al*., Investigating the electrophysiological basis of resting state networks using magnetoencephalography. *Proc. Natl. Acad. Sci. U.S.A.* **108**, 16783–16788 (2011).
80. A. Zhigalov, G. Arnulfo, L. Nobili, S. Palva, J. M. Palva, Modular co-organization of functional connectivity and scale-free dynamics in the human brain. *Network Neurosci.* **1**, 143–165 (2017).
81. R. Hindriks, P. K. B. Tewarie, Dissociation between phase and power correlation networks in the human brain is driven by co-occurrent bursts. *Commun. Biol.* **6**, 286 (2023).
82. F. Siebenhühner, J. M. Palva, S. Palva, Linking the microarchitecture of neurotransmitter systems to large-scale MEG resting state networks. *iScience* **27**, 111111 (2024).
83. J. S. Damoiseaux, M. D. Greicius, Greater than the sum of its parts: A review of studies combining structural connectivity and resting-state functional connectivity. *Brain Struct. Funct.* **213**, 525–533 (2009).
84. L. E. Suárez, R. D. Markello, R. F. Betzel, B. Misic, Linking structure and function in macroscale brain networks. *Trends Cogn. Sci.* **24**, 302–315 (2020).
85. Z. Q. Liu, G. Shafiei, S. Baillet, B. Misic, Spatially heterogeneous structure-function coupling in haemodynamic and electromagnetic brain networks. *NeuroImage* **278**, 120276 (2023).
86. G. Deco *et al*., Rare long-range cortical connections enhance human information processing. *Curr. Biol.* **31**, 4436–4448.e5 (2021).
87. H. Lee *et al*., Relationship of critical dynamics, functional connectivity, and states of consciousness in large-scale human brain networks. *NeuroImage* **188**, 228–238 (2019).
88. S. Gu *et al*., Controllability of structural brain networks. *Nat. Commun.* **6**, 8414 (2015).
89. C. W. Lynn, D. S. Bassett, The physics of brain network structure, function and control. *Nat. Rev. Phys.* **1**, 318–332 (2019).
90. C. Tu *et al*., Warnings and caveats in brain controllability. *NeuroImage* **176**, 83–91 (2018).
91. P. Srivastava *et al*., Models of communication and control for brain networks: Distinctions, convergence, and future outlook. *Network Neurosci.* **4**, 1122–1159 (2020).
92. E. Nozari *et al*., Macroscopic resting-state brain dynamics are best described by linear models. *Nat. Biomed. Eng.* **8**, 68–84 (2023).
93. O. Shriki *et al*., Neuronal avalanches in the resting MEG of the human brain. *J. Neurosci.* **33**, 7079–7090 (2013).
94. F. Castaldo *et al*., Multi-modal and multi-model interrogation of large-scale functional brain networks. *NeuroImage* **277**, 120236 (2023).
95. V. Priesemann, Spike avalanches in vivo suggest a driven, slightly subcritical brain state. *Front. Syst. Neurosci.* **8**, 108 (2014).
96. T. Bellay, A. Klaus, S. Seshadri, D. Plenz, Irregular spiking of pyramidal neurons organizes as scale-invariant neuronal avalanches in the awake state. *eLife* **4**, e07224 (2015).
97. S. A. Jones, J. H. Barfield, V. K. Norman, W. L. Shew, Scale-free behavioral dynamics directly linked with scale-free cortical dynamics. *eLife* **12**, e79950 (2023).
98. A. J. Fontenele, J. S. Sooter, V. K. Norman, S. H. Gautam, W. L. Shew, Low-dimensional criticality embedded in high-dimensional awake brain dynamics. *Sci. Adv.* **10**, eadj9303 (2024).
99. A. Levina, V. Priesemann, Subsampling scaling. *Nat. Commun.* **8**, 15140 (2017).
100. J. Touboul, A. Destexhe, Power-law statistics and universal scaling in the absence of criticality. *Phys. Rev. E* **95**, 012413 (2017).
101. A. Destexhe, J. D. Touboul, Is there sufficient evidence for criticality in cortical systems? *eNeuro* **8**, ENEURO.0551-20.2021 (2021).
102. D. Toker *et al*., Consciousness is supported by near-critical slow cortical electrodynamics. *Proc. Natl. Acad. Sci. U.S.A.* **119**, e2024455119 (2022).
103. S. Vanhatalo *et al*., Infraslow oscillations modulate excitability and interictal epileptic activity in the human cortex during sleep. *Proc. Natl. Acad. Sci. U.S.A.* **101**, 5053–5057 (2004).
104. S. Monto, S. Palva, J. Voipio, J. M. Palva, Very slow EEG fluctuations predict the dynamics of stimulus detection and oscillation amplitudes in humans. *J. Neurosci.* **28**, 8268–8272 (2008).
105. T. Hiltunen *et al*., Infra-slow EEG fluctuations are correlated with resting-state network dynamics in fMRI. *J. Neurosci.* **34**, 356–362 (2014).
106. A. Capilla *et al*., The natural frequencies of the resting human brain: An MEG-based atlas. *NeuroImage* **258**, 119373 (2022).
107. V. Myrov *et al*., Rhythmicity of neuronal oscillations delineates their cortical and spectral architecture. *Commun. Biol.* **7**, 405 (2024).
108. T. Donoghue *et al*., Parameterizing neural power spectra into periodic and aperiodic components. *Nat. Neurosci.* **23**, 1655–1665 (2020).
109. V. Myrov, Hierarchical Kuramoto. GitHub. https://github.com/palvalab/hierarchical_kuramoto_zero. Deposited 3 December 2025.